

# Journal of Biomedical Optics

BiomedicalOptics.SPIEDigitalLibrary.org

## Shape-based reconstruction for transrectal diffuse optical tomography monitoring of photothermal focal therapy of prostate cancer: simulation studies

Robert A. Weersink  
Sahil Chaudhary  
Kenrick Mayo  
Jie He  
Brian C. Wilson

**SPIE.**

Robert A. Weersink, Sahil Chaudhary, Kenrick Mayo, Jie He, Brian C. Wilson, "Shape-based reconstruction for transrectal diffuse optical tomography monitoring of photothermal focal therapy of prostate cancer: simulation studies," *J. Biomed. Opt.* **22**(4), 045004 (2017), doi: 10.1117/1.JBO.22.4.045004.

# Shape-based reconstruction for transrectal diffuse optical tomography monitoring of photothermal focal therapy of prostate cancer: simulation studies

Robert A. Weersink,<sup>a,b,c,d,\*</sup> Sahil Chaudhary,<sup>e</sup> Kenrick Mayo,<sup>e</sup> Jie He,<sup>e</sup> and Brian C. Wilson<sup>c,e,f</sup>

<sup>a</sup>University of Toronto, Department of Radiation Oncology, Toronto, Ontario, Canada

<sup>b</sup>University of Toronto, Institute of Biomaterials and Biomedical Engineering, Toronto, Ontario, Canada

<sup>c</sup>University Health Network, Techna Institute, Toronto, Ontario, Canada

<sup>d</sup>University Health Network, Radiation Medicine Program, Toronto, Ontario, Canada

<sup>e</sup>University of Toronto, Department of Medical Biophysics, Toronto, Ontario, Canada

<sup>f</sup>University Health Network, Ontario Cancer Institute, Toronto, Ontario, Canada

**Abstract.** We develop and demonstrate a simple shape-based approach for diffuse optical tomographic reconstruction of coagulative lesions generated during interstitial photothermal therapy (PTT) of the prostate. The shape-based reconstruction assumes a simple ellipsoid shape, matching the general dimensions of a cylindrical diffusing fiber used for light delivery in current clinical studies of PTT in focal prostate cancer. The specific requirement is to accurately define the border between the photothermal lesion and native tissue as the photothermal lesion grows, with an accuracy of  $\leq 1$  mm, so treatment can be terminated before there is damage to the rectal wall. To demonstrate the feasibility of the shape-based diffuse optical tomography reconstruction, simulated data were generated based on forward calculations in known geometries that include the prostate, rectum, and lesions of varying dimensions. The only source of optical contrast between the lesion and prostate was increased scattering in the lesion, as is typically observed with coagulation. With noise added to these forward calculations, lesion dimensions were reconstructed using the shape-based method. This approach for reconstruction is shown to be feasible and sufficiently accurate for lesions that are within 4 mm from the rectal wall. The method was also robust for irregularly shaped lesions. © 2017 Society of Photo-Optical Instrumentation Engineers (SPIE) [DOI: [10.1117/1.JBO.22.4.045004](https://doi.org/10.1117/1.JBO.22.4.045004)]

Keywords: diffuse optical tomography; interstitial photothermal therapy; prostate focal therapy.

Paper 170043R received Jan. 19, 2017; accepted for publication Mar. 17, 2017; published online Apr. 6, 2017.

## 1 Introduction

Management options for patients with low- or intermediate-risk prostate cancer are either watchful waiting [active surveillance (AS)], in which the cancer is monitored without treatment until there are signs of progression, or radical treatment (prostatectomy or radiation therapy) to remove/destroy the entire prostate gland. While AS has no toxicity, the lack of active treatment incurs risk of progression that leads to a significant dropout rate to active treatment.<sup>1</sup> On the other hand, radical whole-prostate treatments carry a risk of significant complications, such as impotence, incontinence, and bowel dysfunction.<sup>2</sup> This dichotomy has recently encouraged the development of prostate focal therapy in which the dominant “index” lesion, which is associated with the highest risk of extraprostatic spread of disease,<sup>3</sup> is ablated. The objective is to achieve acceptable tumor control with minimal morbidity,<sup>3–5</sup> so the treatment can be repeated if and when new index lesions appear over time. Focal therapy options include high-intensity focused ultrasound,<sup>6,7</sup> cryotherapy,<sup>8,9</sup> radiofrequency ablation,<sup>3,10</sup> and photothermal therapy (PTT).<sup>11,12</sup> Regardless of the modality, successful focal therapy requires real-time monitoring to ensure both complete coverage of the target volume (tumor plus

margin) and safety of critical normal structures, especially the rectum where damage can result in serious fistulas.

Our recent and ongoing clinical trials using PTT use near-infrared (NIR) light from a diode laser delivered into the identified index lesion (+ margin) through one or more interstitial optical fibers to destroy the target tumor by thermal coagulation ( $> \sim 55^\circ\text{C}$ ).<sup>12,13</sup> The initial treatment platform used magnetic resonance imaging (MRI) to identify the lesion and three-dimensional (3-D) transrectal ultrasound to guide fiber insertion, with point temperature sensors monitoring treatment progression.<sup>12</sup> More recently, MRI has been used for needle guidance, with MR thermometry used as a surrogate for directly monitoring the tissue coagulation.<sup>14</sup> This approach is more complex in practice and is resource intensive. Additionally, artifacts and noise in the MR thermometry limit its accuracy, which has led to undertreatment in about one-third of cases to avoid risk of rectal wall damage. Hence, direct monitoring of the coagulation front as it approaches the rectal wall remains a critical unmet need.

We are developing a transrectal diffuse optical tomography (DOT) system as a method for assessing the location and size of the photothermal lesion(s) in near-real time, based primarily on changes in light scattering that are associated with coagulation.<sup>15,16</sup> The clinical objective is to track the location

\*Address all correspondence to: Robert A. Weersink, E-mail: [robert.weersink@rmp.uhn.on.ca](mailto:robert.weersink@rmp.uhn.on.ca)

of the boundary of the growing coagulation zone, which is typically sharply delineated. The posterior border of the coagulation zone is particularly important because of the risk of damage to the rectal wall; thus, we have set an accuracy of  $\pm 1$  mm for localization of this border, based on clinical relevance. This geometry and clinical objective represent a new and unique challenge that, to our knowledge, has not been investigated previously in DOT. The work of Piao and colleagues<sup>17–20</sup> using transrectal DOT was focused on tumor detection, not on interventional guidance, and was based mainly on changes in optical absorption of tumor compared to normal prostate tissue.

We previously used the transrectal probe DOT system of Piao et al.<sup>17</sup> to measure tissue-simulating phantoms containing different sizes of highly scattering cylindrical inclusions, as well as numerical simulations using finite element calculations based on the diffusion equation.<sup>16</sup> This study demonstrated the sensitivity of the DOT signals to the diameter of the inclusion and, hence, of the distance between the nearest inclusion boundary and the DOT source–detector array. Multiple DOT source–detector configurations were simulated to determine the geometries with the highest location sensitivity. DOT signals using source–detector separations ranging from 6 to 20 mm changed by  $\sim 8\%$  per mm in the boundary-to-probe distance as the lesion approached the DOT probe. At smaller source–detector separations in the 2- to 6-mm range, the detected signal tended to first increase then decrease as the lesion boundary approached the mucosal rectal wall. However, in that study, we did not attempt actual 3-D reconstruction of the coagulation zone.

As is well known, DOT reconstruction is an ill-posed inverse problem, so multiple solutions that provide essentially the same measured signals can be found. Typically, this ambiguity can be resolved by employing either spectral reconstruction<sup>21–23</sup> using multiple wavelengths and fitting the concentrations of specific tissue chromophores (water, hemoglobin) and/or using prior geometrical constraints and optimizing the optical properties of each defined region.<sup>24–26</sup> For our specific treatment-monitoring scenario, these standard methods of constraining the reconstruction are not applicable; tissue scattering is not strongly wavelength sensitive (compared to absorption) and the lesion shape is continually changing, negating the application of spatial priors. However, other information-specific treatment monitoring can be used to constrain the DOT reconstruction. First, the boundary between the higher-scattering coagulated tissue and the normal tissue is less than 1 mm.<sup>12</sup> Second, the boundary must grow monotonically during the treatment, so the  $i$ 'th reconstructed coagulated zone must be larger than or equal to the  $(i - 1)$ 'th zone. In this study, we focus primarily on the first characteristic by developing and evaluating a shape-based image reconstruction method and show the utility of the second characteristic in accurate reconstructions for typical treatments. Instead of reconstructing by adjusting the optical properties at each node or within a fixed defined region, shape-based reconstruction methods adjust parameters that define the “shape” of a region, with the assumption that the optical properties within the shape are homogeneous. Shape-based reconstruction methods in DOT have been previously developed using either (a) algebraic functions to define the geometry, including so-called “level sets” in which one or more parameters have fixed values during the reconstruction or (b) a spherical harmonic basis set in which the coefficients are adjusted until the reconstructed shape of a target region corresponds to the true anatomical shape.<sup>27–29</sup> These techniques are better able

to resolve complex structural detail than standard pixel-based reconstruction methods.

Here, we describe the implementation of a shape-based approach to DOT reconstruction using only a small number of fitting parameters that are specific to localizing the boundary of the growing photothermal lesion in focal prostate cancer PTT. Initially, we assume that the photothermal lesion is centered on the treatment fiber, with its long axis parallel to this, and grows as an ellipsoid that is symmetric about its short axis. The position of the treatment fiber relative to the tumor target and rectal wall is known from, e.g., MRI and/or ultrasound imaging. We performed forward simulations of the photothermal lesions and reconstructed them using the shape-based algorithm. Several variations were tested, including: (i) increased noise in the simulated DOT measurements, (ii) optimization of lesion optical properties, (iii) different gradients of the boundary between native and coagulated tissue, and (iv) irregularly shaped lesions. Finally, we examined the feasibility of using shape-based DOT (SBDOT) to reconstruct an actual photothermal lesion in a patient generated using two interstitial treatment fibers.

## 2 Methods

In this section, we first describe the SBDOT reconstruction method for the case of a photothermal lesion created using a cylindrically diffusing fiber and centered about the treatment fiber. The shape of the lesion is described by an ellipsoid function, using the dimensions in the transverse and longitudinal directions to define the geometry. The optical properties within the lesion are assumed to be homogeneous. Reconstruction of the lesion size using diffuse optical measurements is based on adjustment of the shape parameters.

We then outline a series of tests of the shape-based reconstruction that are important in its potential clinical implementation. Simulated measurements were generated using forward calculations of the diffuse optical signals in a model that includes the prostate and rectum as well as photothermal lesions of known size and optical properties, varying the level of added noise. The simulated data were then reconstructed using the shape-based algorithm and the reconstructed lesion geometry and optical properties compared to the true values used in the forward simulation.

### 2.1 Shape-Based Diffuse Optical Tomography Reconstruction Algorithm

All calculations described below were performed in MATLAB® (Mathworks, Massachusetts) using NIRFAST for the forward calculations of the steady-state light distribution, which is based on diffusion theory to describe light propagation in optically turbid media.<sup>21</sup> The anatomy was modeled as a 3-D mesh [Fig. 1(a)], including the prostate, rectal wall, and surrounding tissue, with the prostate model based on clinical MRI images. Figure 1(b) shows the two different transrectal DOT source–detector geometries investigated. In both cases, the fibers are attached to the transrectal probe such that they come in contact with the mucosal rectal wall. Hence, in the axial geometry, the fiber probes follow the curvature of an endorectal probe with a diameter of 25 mm. The mesh density was set to 0.5 mm between nodes in the rectal wall and prostate and 1.0 mm between nodes in the surrounding region. Each region was assigned optical properties matching the best available measurements at  $\sim 750$  nm, as given in Table 1. Optical properties of the rectum vary across studies and are based primarily on *ex vivo*

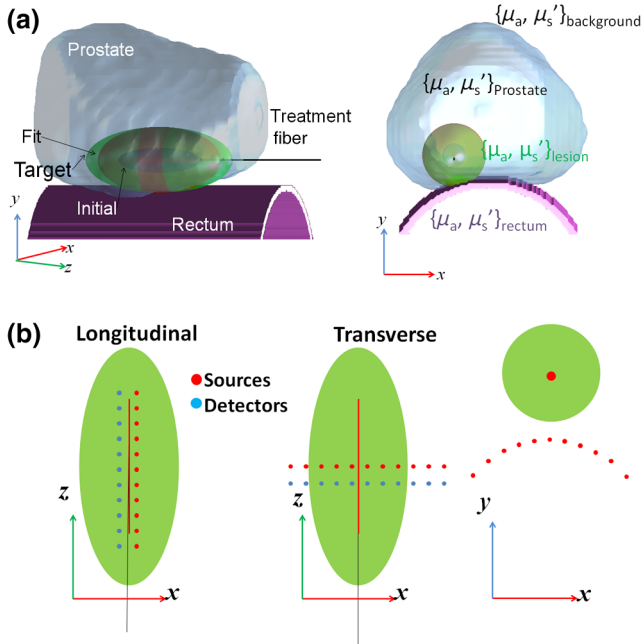


**Fig. 1** (a) Setup for simulations comprising a cylindrical rectum, prostate with shape derived from clinical images, and surrounding tissue. A cylindrically diffusing treatment fiber is longitudinally inserted into the prostate. An ellipsoidal photothermal lesion is centered around the treatment fiber, giving four tissue regions each with its own set of absorption and reduced scattering properties. (b) Transrectal DOT is based on a row of point sources and a parallel row of detectors 2 mm away. Source–source and detector–detector separations within each row are 1 mm. Two configurations are shown: longitudinal in the direction of the treatment fiber and transverse. The transverse view is also shown in the plane of the source fibers, showing that they and the detector fibers follow along the mucosal wall of the rectum. For each configuration, the set of sources and detectors is centered around the treatment fiber.

**Table 1** Optical properties for each tissue type used in the simulations.

Tissue	Native prostate <sup>29,30</sup>	Coagulated prostate <sup>34–37</sup>	Rectum <sup>27,28</sup>	Background
$\mu_a$ (mm <sup>-1</sup> )	0.02	0.02	0.007	0.01
$\mu_s'$ (mm <sup>-1</sup> )	1.0	3.0	1.2	0.70

measurements,<sup>30,31</sup> while human prostate properties have been measured using interstitial methods.<sup>32,33</sup> The optical properties of coagulated prostate tissue have not been reported, so we used scattering contrast similar to that observed with other tissues.<sup>34–37</sup>

### 2.1.1 Photocoagulation lesion definition

The photocoagulation lesion was simulated by identifying nodes within a region defined by the shape function. The lesion generated by the linearly diffusing treatment optical fiber was assumed to be an ellipsoid with radial symmetry transverse to the treatment fiber, where the treatment fiber is oriented parallel to the z-axis. The lesion can thus be written in spherical coordinates as

$$\frac{r^2 \cos^2 \theta \sin^2 \varphi}{a^2} + \frac{r^2 \sin^2 \theta \sin^2 \varphi}{b^2} + \frac{r^2 \cos^2 \varphi}{c^2} = 1, \quad (1)$$

$$\frac{abc}{\sqrt{a^2 b^2 \cos^2 \varphi + a^2 c^2 \sin^2 \theta \sin^2 \varphi + b^2 c^2 \cos^2 \theta \sin^2 \varphi}} = r, \quad (2)$$

where  $a = b \neq c$  and  $r$  is the distance of each node from the center of the ellipsoid. The length of the vector from the lesion center to a point on the coagulation lesion boundary is  $R$ , so, if  $r < R$ , then the node is within the ellipsoid and is included within the region used to define the lesion. Once the region is defined, its optical properties are set to match those of coagulated tissue.

If the treatment fiber is not parallel to the z-axis, then the coordinates found above can be rotated using standard methods to align with the treatment fiber. Using the rotation matrix between the z-axis and treatment fiber direction, each node in the mesh can be first rotated and then tested to determine if it is within the ellipsoid.

### 2.1.2 Forward calculation of diffuse optical tomography signals

Having thus defined the coagulation lesion within the normal tissue anatomy, NIRFAST was used to calculate the resulting optical signals that would be expected using the transrectal DOT probe. Assuming steady-state conditions,  $\Phi_{ij}$  is the signal amplitude between each source ( $i$ ) and detector ( $j$ ) pair, separated by distance  $\rho_{ij}$ . In the configurations tested here, the minimum and maximum source–detector separations are 2 and 20 mm, respectively, with a required dynamic range of 10 orders of magnitude. Our assembled system uses variable-gain photomultiplier tubes that are able to cover this range of signals. In our previous study,<sup>16</sup> we found that, as the lesion expands during treatment, the change in signal amplitude was  $\Delta\Phi_{ij} \sim -8\%$  per mm (i.e., decreases) at large source–detector separations, while at small source–detector separations,  $\Phi_{ij}$  first increases then decreases as the coagulation zone grows. While the convention in DOT is to use  $\log(\Phi_{ij})$  as the signal in the optimization process, we found that this inadequately accounted for the important changes in  $\Phi_{ij}$  at small  $\rho_{ij}$  during the shape-fitting optimization and overweighted the data at large source–detector separation. Instead, we found empirically that  $\Psi_{ij} = \ln(\Phi_{ij})/\rho_{ij}$  optimally balanced the changes in optical signals observed across all source–detector combinations.  $\Psi$  is used to indicate measurements at all source–detector pairs, i.e.,  $\Psi = \{\Psi_{ij}\}$ .

The calculated signal depends on the lesion shape parameters, notated here as  $[B]$ , and the optical properties of the lesion,  $[\mu_a, \mu_s']$ . Hence, the signal is written as  $\Psi([B], [\mu_a, \mu_s'])$  to show the various dependencies. A generic shape variable descriptor,  $[B]$ , is used since it is possible in principle to include any shape to describe the lesion. For the ellipsoidal shape used, the shape parameters are the transverse and longitudinal radii as defined in Eqs. (1) and (2), i.e.,  $[B] = [a, c]$  with  $B_1 = a$  and  $B_2 = c$ . The optical properties of the other regions (untreated prostate, rectal wall, and surrounding tissue) are assumed to be constant throughout.

### 2.1.3 Lesion reconstruction

Using the simulated signals as input data and applying the standard Gauss–Newton algorithm for solving nonlinear least-squares problems,<sup>38</sup> the 3-D tomographic reconstruction of the lesion minimizes the following least-squares function:

$$\chi(C) = \frac{1}{m} \sqrt{\|\Psi_M - \Psi_C([B], [\mu_a, \mu_s'])\|^2}, \quad (3)$$

where  $\Psi_M$  is the measured signal,  $\Psi_C$  is the calculated signal following iterative reconstruction, and  $m$  is the number of individual source–detector measurements. The Jacobian for the reconstruction is derived for the elliptical shape parameters and optical properties of the coagulated region as

$$J = \begin{bmatrix} \frac{\partial \Psi_1}{\partial B_1}, & \dots & \frac{\partial \Psi_1}{\partial B_k}, & \frac{\partial \Psi_1}{\partial \mu_a}, & \frac{\partial \Psi_1}{\partial \mu_s'} \\ \vdots & \ddots & \vdots & \vdots & \vdots \\ \frac{\partial \Psi_m}{\partial B_1}, & \dots & \frac{\partial \Psi_m}{\partial B_k}, & \frac{\partial \Psi_m}{\partial \mu_a}, & \frac{\partial \Psi_m}{\partial \mu_s'} \end{bmatrix}, \quad (4)$$

where  $k$  is the number of shape parameters. For ellipsoidal shapes,  $k = 2$ . If the optical properties of the lesion are fixed and hence not included as variables in the reconstruction, then the optical property components of the Jacobian, i.e., the last two columns in Eq. (4), do not need to be included. The shape parameters and optical properties are iteratively updated using

$$(J^T J + \lambda I) \Delta[B, \mu_a, \mu_s'] = J^T (\Psi_c - \Psi_m), \quad (5)$$

$$\Delta[B, \mu_a, \mu_s'] = J^T (\Psi_c - \Psi_m) / (J^T J + \lambda I), \quad (6)$$

$$[B, \mu_a, \mu_s']_{k+1} = [B, \mu_a, \mu_s']_k + \Delta[B, \mu_a, \mu_s'], \quad (7)$$

where  $\Psi_c$  and  $\Psi_m$  are the calculated and measured  $\Psi$ , respectively, and  $\lambda$  is the standard Tikhonov regularization term that decreases with each iteration. The initial values of  $\lambda$  and the rate at which it decreases were determined from initial testing of the optimization and manually set such that a converging solution could be found in almost all cases. The solution was considered to have converged optimally when the value of  $\chi(C)$  from Eqs. (1) and (2) was  $< 0.002$  or when values of  $[B]$  varied by  $< \pm 0.2\%$  between three consecutive iterations. With the first convergence criteria, changes in  $[B]$  were typically  $< 0.2$  mm, which are well within our set clinical tolerance of  $< \pm 1$  mm.

When optimizing the lesion shape and optical properties simultaneously, values of  $[B]$ , i.e., the lesion shape, converged quickly after 4 to 7 iterations, but further iterations were required for the optical properties to converge. However, the resulting solution often corresponded to an incorrect local minimum for both shape and optical properties. To avoid this outcome, a scaling factor,  $sc$ , was included in Eq. (7) to reduce the updating of  $[B]$  with each iteration; thus, Eqs. (5)–(9) were modified as

$$[B]_{i+1} = [B]_i + sc * \Delta[B], \quad (8)$$

$$[\mu_a, \mu_s']_{i+1} = [\mu_a, \mu_s']_i + \Delta[\mu_a, \mu_s']. \quad (9)$$

A value of  $sc \sim 0.3$  was found through multiple tests to provide the best global solutions.

The simulated source and detector positions along the mucosal wall of the rectum were arranged in two parallel rows separated by 2 mm [Fig. 1(b)] and centered about the treatment fiber in the prostate. In each row, neighboring sources/detectors were separated by 1 mm. Two configurations of this arrangement were tested, with the rows aligned either longitudinally (along the rectal axis) or transversely. Both configurations were tested since our previous simulations demonstrated that they were both sensitive to the growing photothermal lesion. In each case, the treatment fiber was placed 10 mm from the DOT probe in contact with the rectal wall.

If full optimization that included both the shape parameters and lesion optical properties was performed, then convergence was typically found within 10 to 15 iterations depending on the initial values of  $[B]$  and  $[\mu_a, \mu_s']$ , the value of  $sc$ , and the level of added noise in the simulated forward data. If the lesion optical properties were fixed and only  $[B]$  was optimized, then  $sc$  was set to unity.

## 2.2 Testing of Reconstruction

The shape-based reconstruction was tested using a series of simulation measurements under several conditions for both the axial and transverse source–detector configurations. The DOT measurements were simulated using forward calculations of known lesion geometries and optical properties, with varying levels of added noise. The resulting reconstructions were then compared to the known geometries, with special attention to the recovered versus true shape parameters and, for some calculations, the recovered versus true optical properties.

### 2.2.1 Standard diffuse optical tomography reconstruction

Standard DOT methods were used to attempt reconstruction of a simulated thermal lesion of 8 mm transverse radius, 12 mm longitudinally, and centered 10 mm from the luminal rectal wall. The optical properties of the various tissues are listed in Table 1. The initial guess was taken as a lesion 3 mm in radius and 7 mm in length since this lesion results in only minor changes to the DOT signal relative to no lesion present and it conforms to the generally expected shape around the treatment fiber. With no shape constraints, reconstruction adjusted both absorption and scattering properties at all vertices of the finite element mesh.

### 2.2.2 Effect of noise and starting conditions

A series of forward calculations were generated for lesions centered at 10 mm from the luminal rectal wall and increasing in transverse radius from  $a = 4$  to 9 mm in 1-mm increments and in long-axis radius from  $c = 8$  to 13 mm. Three potential starting conditions were examined. The first two used a fixed lesion size: one guess assumed a small lesion, with  $B = [3, 7]$  mm, while the other used an initial guess at the maximum lesion diameter of  $B = [10, 20]$  mm. The forward calculations were reconstructed using each initial guess for the reconstruction.

A third starting condition simulated a standard photothermal treatment in which lesion size increases as the treatment progresses. Hence, forward calculations were generated for a series of lesions increasing in transverse radius from  $a = 4$  to 9 mm in 1-mm increments, which corresponds to the distance between the treatment fiber and the mucosal rectal wall decreasing from 6 to 1 mm. The long-axis radius was concurrently

increased from  $c = 8$  to 13 mm. The initial guess for the first reconstruction was  $[B] = [3, 7]$  mm, and, during successive reconstructions, the shape parameters from the previous lesion were used as the initial values, i.e.,  $[B]_j^{\text{fit}} = [B]_{j+1}^{\text{initial}}$ .

To examine the impact of measurement noise on the reconstruction accuracy, the noise was assumed to be Gaussian and added to each of the simulated measurements ranging between 0% and 20% in increments of 2%. The simulated measurements and reconstructions were repeated five times for each of the seven lesion sizes and the reconstructed values for each lesion size were then averaged and their ranges noted.

### 2.2.3 Effect of fitting optical properties

The above tests of the expanding lesion were repeated including optimization of the lesion optical properties. While the actual lesion properties were  $[\mu_a, \mu_s]_l = [0.02, 3.0]$  mm<sup>-1</sup>, four sets of initial optical property guesses were tested in the reconstructions with  $\mu_{a,\text{Guess}} = 0.01$  or  $0.04$  mm<sup>-1</sup> and  $\mu'_{s,\text{Guess}} = 1.5$  or  $5.0$  mm<sup>-1</sup>, using all four possible combinations of these properties.

### 2.2.4 Lesion boundary gradient

The shape-based reconstruction assumes a sharp boundary between regions of different optical properties. While histopathology indicates a clear boundary between native and coagulated tissue, the tissue scattering depends on extracellular matrix protein denaturation as well as purely cellular properties, so there may be an effective gradient in optical scattering coefficient across the lesion boundary. Hence, a sigmoidal boundary function was applied to the ellipsoidal lesion and the forward calculations compared with those for a sharp boundary, with lesions of different sizes diameters. The sigmoid function was

$$S(r) = (\mu'_{s,\text{coag}} - \mu'_{s,\text{nat}}) \frac{1}{\left\{ 1 + \exp \left[ -\frac{9(r_c - r)}{\text{width}} \right] \right\}} + \mu'_{s,\text{nat}}, \quad (10)$$

where *coag* and *nat* refer to the coagulated and native tissues, respectively, *width* is the width of the gradient between its 10th and 90th percentile values,  $r_c$  is calculated from Eqs. (1) and (2) for the basis ellipsoid, and  $r$  is calculated for the surrounding nodes based on Eq. (10). The tissue scattering properties were modified only for nodes where  $|r_c - r| < \text{width}/2$ . An initial lesion was created with  $[B] = [6.5, 11]$  and centered 10 mm from the mucosal rectal wall. The width of the gradient was varied from 0 to 3 mm in 0.25-mm increments, and forward calculations were performed for each lesion with  $a$  ranging from 6 to 8.5 mm in 0.1-mm increments. The least-squares difference between the forward calculations of the gradient ( $\text{width} > 0$ ) and sharp ( $\text{width} = 0$ ) lesions was calculated, similar to Eq. (3).

### 2.2.5 Irregularly shaped lesions

While the photocoagulation lesions generated during interstitial PTT are generally symmetric about the source fiber(s), variations are seen clinically due to local variations in tissue blood perfusion that affect light transport and/or heating. Hence, irregularly shaped coagulation zones were modeled by adding a series of spherical harmonics to the ellipsoid. Thus, we used

a complete basis set of spherical harmonics,  $Y_l^m$ , into which the 3-D shapes of the lesion could be expanded. Spherical harmonics of degree  $l$  and order  $m$  are defined as

$$Y_l^m(\theta, \varphi) = N_l^{|m|} P_l^{|m|} \cos(\theta) e^{im\varphi}, \quad (11)$$

where  $P_l^{|m|}$  denotes Legendre polynomials and  $N_l^{|m|}$  is a normalization coefficient defined as

$$N_l^{|m|} = \sqrt{\frac{2l+1}{4\pi} \frac{(l-m)!}{(l+m)!}}. \quad (12)$$

Any real spherical function,  $f(\theta, \varphi)$ , can be expanded in the form

$$f(\theta, \varphi) = \sum_{l=0}^{\infty} \sum_{m=-l}^l C_l^m Y_l^m(\theta, \varphi), \quad (13)$$

where  $C_l^m$  is the coefficient defining the relative contribution of each harmonic function to the surface function,  $f$ , which was calculated using 50 spherical harmonics with each coefficient  $C_l^m$  randomly generated between  $\pm 0.5$ .

The values of  $f$  and  $r$  [from Eq. (2)], together with the length of the vector from the ellipsoid center to the node,  $R$ , were calculated for each node. The global contribution of the spherical harmonics to the lesion shape was scaled, so the level of irregularity could be increased systematically. An irregularity scaling factor to quantify this was defined as  $v = 2 \times \sigma(f)$ , i.e., twice the standard deviation of  $f$ , ranging from 0.25 to 3.0 mm. If  $R > (r + v \times f)$ , then the node was included within the region used to define the lesion. Forward models were generated, and 5% noise added. The resulting data were then fitted to the simple ellipsoid model. The goodness of fit was characterized by comparing the distance between the mucosal rectal wall and nearest 2 mm<sup>2</sup> surface area on both the irregular lesion and the fitted ellipsoid; for the lesion meshes, this 2 mm<sup>2</sup> area could be approximated by measuring the average distance of the 20 nodes closest to the rectal wall. This process was repeated 50 times for each scale factor with randomly varied harmonic coefficients, and the values were then averaged. The large number of simulations was required because our primary interest is knowing approximately how many times the shape-based fit does not capture the possibility of a small part of the photothermal lesion expanding into the rectum. This was assessed by calculating at each irregularity scaling level the average difference between the nearest 2 mm<sup>2</sup> of the irregular shape to the mucosal rectal wall and the same location determined by the shape-based reconstruction. The standard deviation of this difference was also calculated at each irregularity scaling level. Two times the standard deviation represents the maximum expected error in  $\sim 95\%$  of the cases. Hence, the fitting method would be considered unsafe when the average difference plus  $2\sigma$  has a value greater than 1 mm since this would mean that in more than 1/20 of the cases, the reconstruction will not accurately predict the extent of the photothermal lesion.

### 2.2.6 Clinical lesion

The shape-based reconstruction was used to fit a clinical case comprising a coagulation zone identified using Gadolinium-enhanced contrast MRI at 7 days after PTT treatment of a patient with focal prostate cancer.<sup>39</sup> While transrectal DOT was not performed, this case was used to simulate a realistic geometry for

PTT-generated lesions in the prostate. A finite element mesh was generated to outline the prostate and lesions, and the same source–detector configurations were used to simulate the DOT measurements. The photothermal lesion volume was generated using two parallel diffusing fibers each 20-mm long, separated transversely by 10 mm and longitudinally by 7 mm, as identified on the MR images. The posterior end of the PTT lesion was partially located outside the prostate in this patient, but, for modeling purposes, it was moved to be fully within the prostate. The centers of the reconstructed lesions were set by the positions of the treatment fibers, as located by MRI. The rectum was remodeled as a cylinder, as in Fig. 1. Considering the limited overlap between each of the treatment zones from the two fibers, two separate sequential treatments were modeled. The simulated DOT probe was positioned on the mucosal rectal wall, so the distance between the center of the DOT fiber array and the center of each treatment fiber was minimized. Hence, the probe position was different for the two treatments. The tissue optical properties were assumed to be as in Table 1.

### 3 Results

#### 3.1 Standard Reconstruction

The initial guess in the standard DOT reconstruction assumed a small, highly scattering lesion with a transverse radius of 3 mm and centered 10 mm from the mucosal rectal wall. The target lesion had the same optical properties with transverse radius  $a = 8$  mm, as shown in Figs 2(a) and 2(c). Here, the absorption properties of the lesion are the same as the prostate, while the reduced scattering was higher (3 versus  $1 \text{ mm}^{-1}$ ) in the rest of the prostate. The standard DOT reconstruction produces a region of high absorption just anterior of the rectal wall [Fig. 2(b)] and slightly increased scattering at the lesion center [Fig. 2(d)]. No clear lesion boundary can be identified in either the absorption or scattering profiles. The reconstructions are

obviously inaccurate, and such results would have little utility in treatment monitoring.

#### 3.2 Shape-Based Diffuse Optical Tomography; Effect of Noise and Starting Conditions

We first consider the impact of the initial guess in the shape-based reconstruction and the effect of added noise on the reconstruction accuracy. Two initial guesses were considered: a very small lesion with  $B = [3,7]$  and a very large lesion with  $B = [10,20]$ . Figures 3(a) and 3(b) show that the former leads to significant difficulty in accurately reconstructing the lesions even with no added noise; for example, in the longitudinal DOT configuration, reconstruction of the 9-mm-radius lesion fails completely. When using initial guess of  $B = [3,7]$ , noise at 4% to 6% of the signal already adversely affects the reconstructions. Using an initial guess of  $B = [10,20]$  enables more accurate reconstructions for lesions with  $a = 5$  to 9 mm [Figs. 3(a) and 3(b)], which is the region of primary clinical interest. The reconstructions are also more robust against noise and the lesions' shapes can be accurately reconstructed for  $a = 5$  to 9 mm with 10% noise [Figs. 3(c) and 3(d)] and up to 16% for  $a = 7$  to 9 mm (results not shown). The poor results reconstructing larger lesions when using a small lesion as the initial guess may be due to the nonlinear response of the DOT signal with increased scattering. As noted earlier, in both measured and simulated data, the signal at small source–detector separations first increases then decreases as the lesion grows. Since the Jacobian does not reflect this change at the start of the reconstruction, the reconstructions do not converge.

#### 3.3 Expanding Lesions and the Effect of Noise on Reconstruction Accuracy

In interstitial fiber-based photothermal treatment, the lesion grows continuously. To simulate a typical treatment, we used

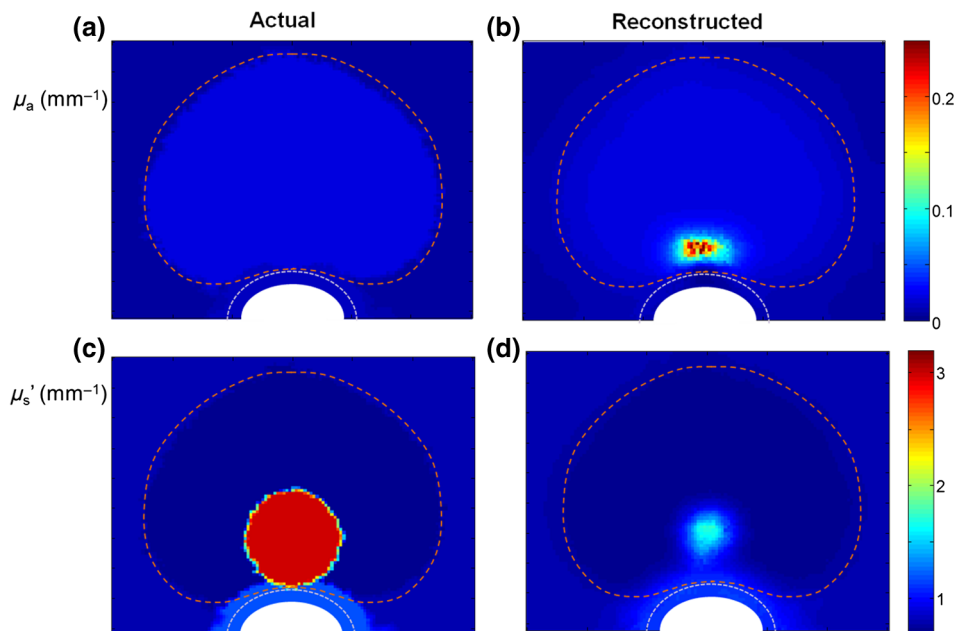


**Fig. 2** Results of standard (nonshape based) DOT reconstruction of a photothermal lesion with high scattering. (a, c) Actual optical properties and (b, d) reconstructed properties. The dashed lines show contours of the prostate (red) and outer rectal wall (white).

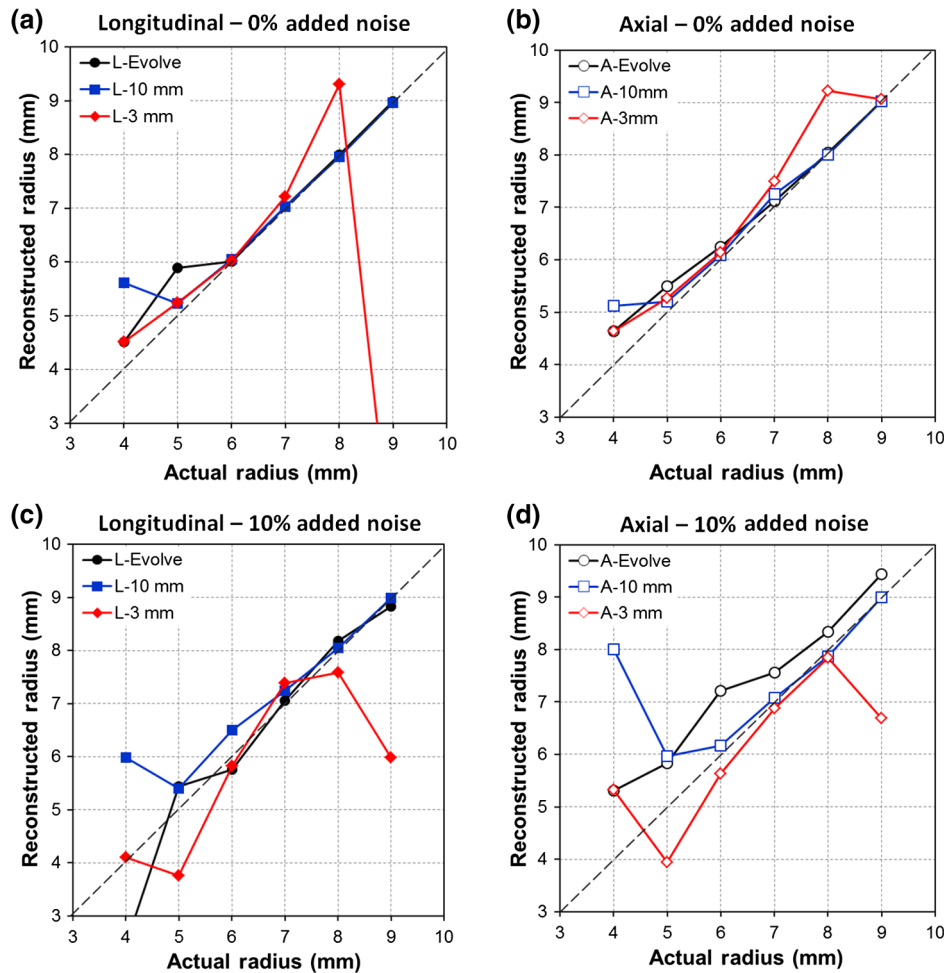


**Fig. 3** Transverse reconstructions (a, c) longitudinal and (b, d) transverse source-detector configurations for different levels of added noise: (a, b) 0%, (c, d) 10%. Three different fitting tests are shown. Those labeled 10 and 3 mm use starting conditions for each fit of 10 and 3 mm, respectively, for the transverse axis and 20 and 7 mm for the longitudinal axis. Data labeled evolve indicates an expanding lesion in which the initial guess for lesion  $i$  is the best-fit for lesion  $i - 1$ . The starting lesion has an assumed transverse radius of 3 mm. Data represent the means of 5 simulations.

the reconstructed  $(i - 1)$ 'th lesion as the initial value for the  $i$ 'th reconstruction. The result of this constraint is that the reconstructed transverse radius is very close to the true value ( $<1$ -mm difference), even for small lesions that are far from the rectal wall and DOT probe [Figs. 3(a) and 3(b)]. Both probe configurations (longitudinal and transverse) have equally good performance. Fitting of the long axis of the lesions (not shown) is much poorer, even with no noise. This is not surprising since the treatment fiber length is approximately the same length as the line of sources and detectors in the longitudinal configuration and the lesion grows to extend beyond the ends of the treatment fiber. Likewise, the axial configuration under-samples the distal and proximal ends of the lesion.

The accuracy of the reconstructed transverse boundary does deteriorate with added noise in both probe configurations, particularly for smaller lesions ( $a < 6$  mm) in which the posterior boundary is farther from the probe. Nevertheless, for larger lesions ( $a > 7$  mm) that are most clinically relevant, the reconstruction is generally within  $\pm \sim 0.5$  mm up to noise levels of  $\sim 10\%$  and the fits remain stable even at higher noise (results not shown). In current preclinical studies using our in-house probe measuring canine prostates, our measurement error

is within the range of 5% to 10%. Here, measurement noise includes detection noise, position stability of the probe, and contact between the probe and the tissue and assumes that the physiology is constant except for the growing lesion.

The results of fitting both the lesion dimensions and optical properties are shown in Fig. 4, where convergence occurred within 10 to 15 iterations. With no noise, fitting of the small lesions tends to overestimate the lesion size by  $\sim 1$  mm and underestimate both absorption and scattering. This may be the result of trade-off between the fitted optical property values and the fitted lesion size. Attenuation of the DOT signal is affected by the size of the lesion and the increase in lesion absorption and scattering. By starting with an estimate of the tissue attenuation that is lower than the actual optical properties of the lesion, the fitting algorithm may be attempting to fit to the observed attenuation by increasing the lesion size. However, recovery of both the shape and optical properties becomes more accurate as the lesion grows. With increased noise, recovery of both the lesion dimensions and the optical properties begins to fail; for larger lesions, the size is consistently underestimated while the scattering is markedly overestimated, especially for the longitudinal fiber arrangement. As noted earlier,

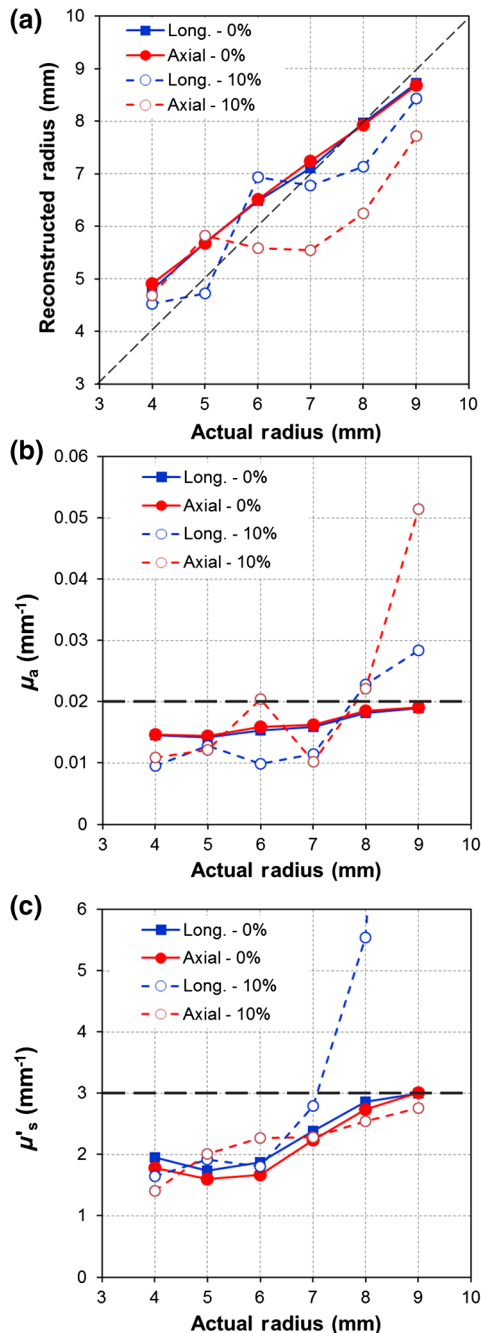


**Fig. 4** Reconstructions for both probe configurations of lesion size (transverse radius) and optical properties for an expanding lesion in which the initial guess for lesion  $i$  is best-fit to lesion  $i - 1$  and the starting values are transverse radius = 3 mm,  $\mu_a = 0.01$  mm<sup>-1</sup> and  $\mu'_s = 1.5$  mm<sup>-1</sup> (actual properties  $\mu_a = 0.02$ ,  $\mu'_s = 3.0$  mm<sup>-1</sup>), and with 0 or 10% added noise. (a) Reconstructed radius versus actual radius, (b) reconstructed absorption coefficient, and (c) reconstructed reduced scattering coefficient. Note that with 10% noise and 9-mm radius, the reconstructed scattering coefficient ( $\mu'_s = 18$  mm<sup>-1</sup>) is not plotted.

there is some trade-off in the reconstruction between the shape parameters and the optical properties, such that reconstruction of the former converges quickly to local minima for any given optical properties. It may be possible to reduce this effect by adjusting the relative scaling in Eq. (8), but this was not tested.

The initial guess of the optical properties had little effect on the reconstruction of the lesion shape [Fig. 5(a)]. Reconstruction

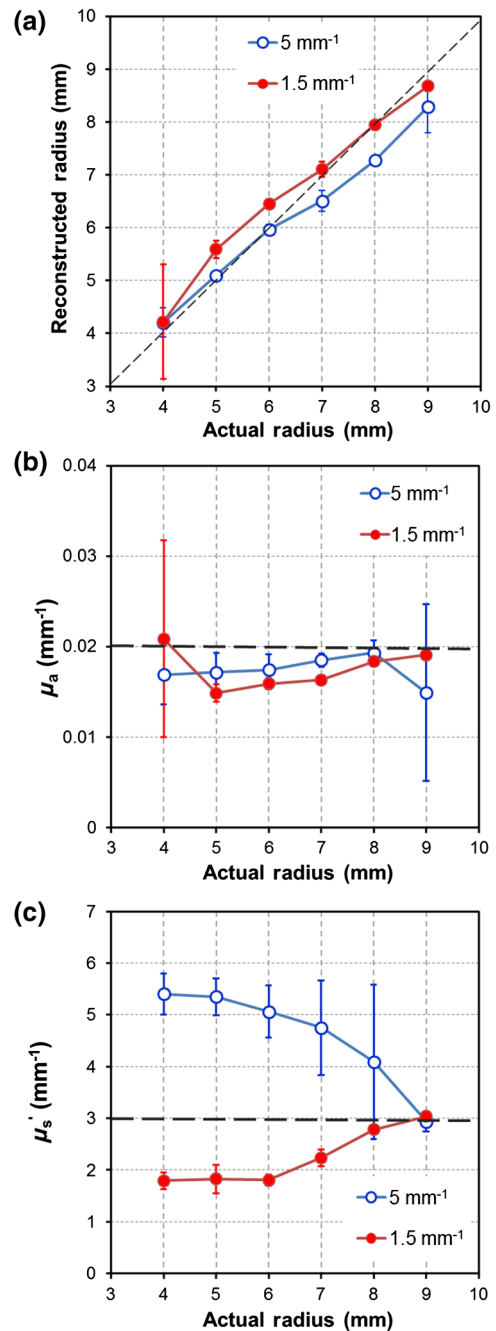


**Fig. 5** Reconstructions of lesion size (transverse radius) and optical properties for an expanding lesion in which the initial guess for lesion  $i$  are best-fit to lesion  $i - 1$  using starting values of transverse radius = 3 mm and a range of optical properties ( $\mu_a = 0.01$  or  $0.04$  mm<sup>-1</sup>;  $\mu'_s = 1.5$  or  $5.0$  mm<sup>-1</sup>). Actual properties  $\mu_a = 0.02$ ,  $\mu'_s = 3.0$  mm<sup>-1</sup>. Data show average results of transverse and longitudinal fiber arrangements for all initial values of  $\mu_a$ . Error bars represent standard deviation across these fits. Reconstructions are separated into two groups based on the initial  $\mu'_s$  guess. (a) Reconstructed radius versus actual radius, (b) reconstructed absorption coefficient, and (c) reconstructed reduced scattering coefficient.

results were similar regardless of fiber arrangement and the initial value of the absorption coefficient. For the absorption coefficient, reconstructed absorption values tended to converge to the correct absorption coefficient of the lesion [Fig. 5(b)]. There was a small dependency on the initial guess of the scattering coefficient, with reconstructions of the transverse radius

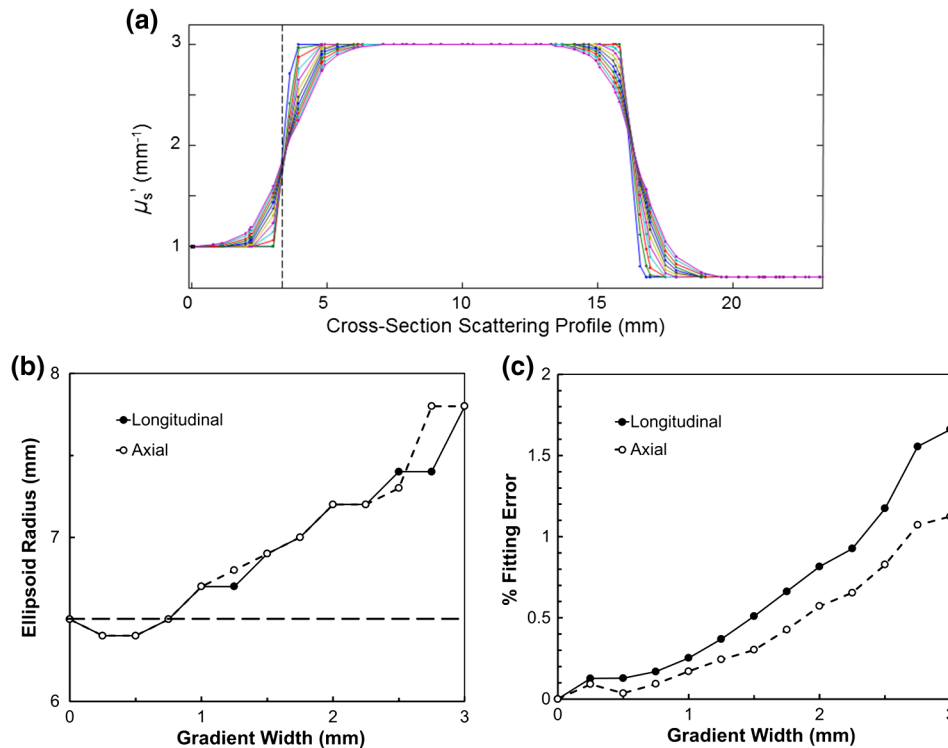


**Fig. 6** Sensitivity of gradient lesion reconstructions based on an initial ellipsoid of 6.5 mm small-axis radius. (a) Profiles of the reduced scattering coefficient from the rectal wall (at 0 mm) through the prostate using increasing levels of gradient [Eq. (10)]. (b) Best-fit ellipsoid radius versus gradient width. Dashed gray line depicts the initial lesion diameter (6.5 mm). (c) Corresponding percentage fitting errors.

smaller than the actual radius when using an initial guess of  $\mu_s' = 5 \text{ mm}^{-1}$  than when the initial scattering guess was  $\mu_s' = 1.5 \text{ mm}^{-1}$ . In all cases, the reconstructed transverse radius was still within our specification of less than 1 mm error. The initial guess of the reduced scattering coefficient did adversely affect the actual reconstruction of the reduced scattering, which tended to match the initial guess of  $\mu_s'$  until the coagulation lesion increased in size [Fig. 5(c)].

### 3.4 Reconstruction with Boundary Gradient

Examples of the scattering profiles from the mucosal rectal wall through the lesion and into the anterior portion of the prostate for the case of a nonsharp photocoagulation boundary are shown in Fig. 6(a). The midpoint of the gradient boundary was fixed at 3.5 mm from the mucosal rectal wall, i.e., a transverse radius of 6.5 mm. Forward calculations for these gradient lesions were compared to forward calculations of ellipsoid lesions of varying transverse radii using a least-squares difference metric. The reconstructed radius is plotted against the boundary gradient width in Fig. 6(b) and the error in the fits in Fig. 6(c). As the gradient width increases, the recovered lesion radius also increases; thus, for a 3-mm gradient width, the closest lesion match has a radius of 8 mm, i.e., a 1.5-mm increase over the sharp-boundary value of 6.5 mm assuming no gradient. This effect is observed in both the axial and longitudinal source-detector fiber configurations. This reconstruction error is larger than our target accuracy of 1 mm. However, this error is systematic, so with validation of the lesion size by other methods (e.g., contrast-enhanced MRI or histopathologic mapping), it can likely be corrected. The results also demonstrate that the DOT

measurements are more sensitive to small changes in scattering closer to the rectal wall than to large changes deep within the tissue. This sensitivity may be useful from a safety perspective since it emphasizes changes closer to the rectum and flags the change in tissue status prior to risking damage to the rectal wall.

### 3.5 Irregularly Shaped Lesions

An example of reconstructing an irregular photocoagulation lesion, with 5% Gaussian noise added prior to reconstruction, is shown in Fig. 7(a). The greatest concern clinically is accurate determination of the distance of the closest lesion boundary from the outer rectal wall. This distance was assessed by considering the distance of a small surface area (2 mm<sup>2</sup>) on the lesion to the rectal wall since this could result in rectal fistula. Since the results were very similar for both source-detector configurations, Fig. 7(b) shows just the transverse case. The shape-based reconstruction systematically underestimates the distance of the nearest 2 mm<sup>2</sup> portion, but the average difference is within the  $\pm 1$  mm tolerance for lesions in which the irregularity scaling is less than 2.5 mm. The error bars on the plot of the difference show 2X the standard deviation and represent the extent of  $\sim 95\%$  of the fits. The average error plus  $2\sigma$  crosses becomes larger than 1 mm at an irregularity scaling of 2 mm. Hence, the fitting method would be considered unsafe at this point since this would mean that in more than 1/20 of the cases, the reconstruction will not accurately predict the extent of the photothermal lesion. From our clinical experience,<sup>12-14</sup> most PTT lesions fall within this degree of irregularity.

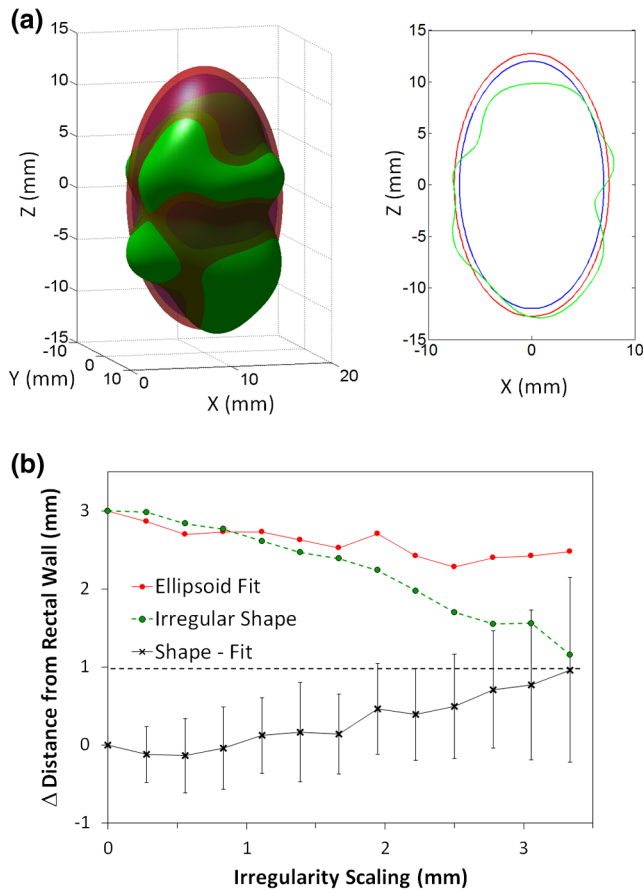


**Fig. 7** (a) Example of irregular lesion showing the base ellipsoid (blue) with  $[B] = [7, 12]$ , the irregular shape generated by adding spherical harmonics (green) and the best ellipsoidal fit to the irregular lesion (red): left: 3-D model with the blue ellipsoid appearing as magenta since it is inside the red lesion; right: cross-sectional view through  $y = 0$ . (b) Comparison of the mean distance over 50 samples of the  $2 \text{ mm}^2$  closest to the mucosal rectal wall for the irregular lesions (green), and ellipsoidal fits (red), and the difference between these fits (black): error bars are  $\pm 2$  standard deviations.

### 3.6 Reconstruction of Clinical Lesion

Results of the reconstructions of the clinical lesion are shown in Fig. 8. The top views in Fig. 8 are posttreatment Gd-contrast MRI showing the prostate (red), the rectum (blue), the photothermal lesion (cyan), and the locations of two treatment fibers (yellow and green). The lower view shows sagittal and axial views of the contours. The photothermal lesion is shown in black while the two shape-based reconstructions are shown in brown for the yellow treatment fiber and purple for the green treatment fiber. Fitting of the superior lesion was successful, with the reconstructed distance to the rectum being within 1 mm of the true contoured lesion. However, the size of the inferior lesion is larger than the actual lesion by 1 to 2 mm, which is somewhat outside the desired uncertainty. This may be due in part to the location of the treatment fiber being offset from the center of the photothermal lesion for this particular case, which is unusual in our clinical experience. This potential problem requires further investigation on a representative range of clinical cases.

## 4 Discussion

We have developed and demonstrated a simple shape-based approach for DOT reconstruction of photothermally generated

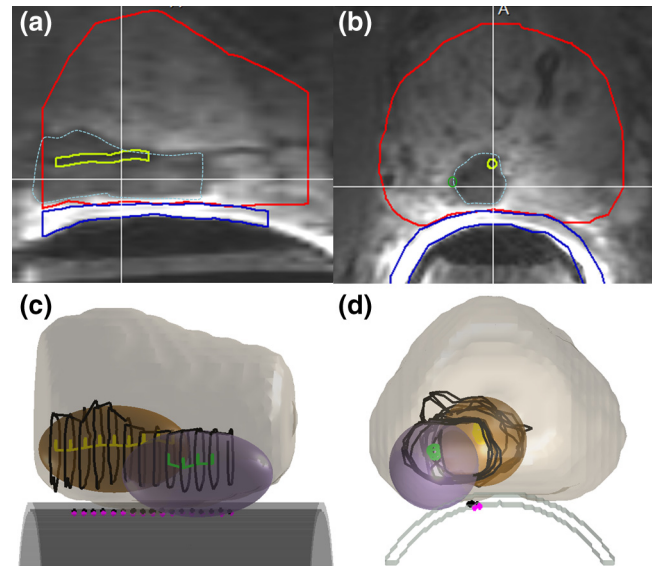


**Fig. 8** Shape-based fitting of photothermal lesion in patient. (a) Sagittal and (b) axial Gd contrast-enhanced MRI images at 7 days after treatment showing the photothermal lesion (contoured in cyan) and the locations of two treatment fibers (yellow and green). (c) Sagittal and (d) transverse surface renderings of the prostate, rectum, location of the sources (black dots), and detectors (magenta dots) on the mucosal rectal wall. Photothermal lesion contours are shown in black. Two ellipsoids were used to reconstruct the lesion; each centered around one of the treatment fibers with sources and detectors also shifted to match these fiber positions. Fitting of the lesion generated by the superior fiber (yellow) closely matches its distance from the rectal wall while fitting of the inferior lesion (green) underestimates the separation.

lesions in the geometry of the prostate using simulated data based on forward calculations. The shape function was selected to match the lesions that are typically seen in patients. The SBDOT method becomes more accurate as the lesion approaches the rectal wall, as required for treatment response monitoring and control. For irregularly shaped lesions, the simple ellipsoid provided a reasonable estimate of the closest extent of the lesion to the rectum and was within our specified error of 1 mm for most irregular shapes. In radiation therapy of prostate cancer, the standard practice is to calculate maximum planned dose to  $1 \text{ mm}^3$  of the rectal tissue. We approximated this metric by measuring the proximity of the closest  $2 \text{ mm}^2$  surface of the lesion to the rectum. For complicated irregular lesions, the shape-based model can be extended to include other shaping parameters. As suggested by Arridge et al.,<sup>27</sup> reconstruction of the lesion could be initiated with a simple shape, such as the ellipsoid, and further improved using several spherical harmonics.

The SBDOT was less accurate in the situation of a gradient (nonsharp) boundary between the lesion and native tissue. However, in our experience from gross pathology and posttreatment Gd-contrast MRI, the boundary is sharper than was modeled here,<sup>13</sup> so the results likely represent the extreme case. Further direct measurements of protein coagulation on preclinical samples following PTT, for example, using second harmonic<sup>40,41</sup> or Raman microscopy,<sup>42</sup> may be needed to measure the actual gradients. It is important to note that the difference between the reconstructed and actual photocoagulation lesion size is systematic, which could then be taken into account in the response treatment monitoring by DOT.

While we have outlined the concept and demonstrated the feasibility of SBDOT, several potential improvements remain to be explored. In this study, the reconstruction used the standard Gauss–Newton method with empirical optimization of the regularization term and the scaling used to optimize fitting of both the optical properties and lesion boundary. We speculate that more sophisticated optimization methods, such as variations of gradient descent methods<sup>43</sup> or evolutionary methods,<sup>44</sup> may yield better results. The impact of initial starting conditions on the reconstruction may require further investigation since it was found that having an initial guess of either a very small or very large lesion had a significant impact on the convergence rate and accuracy of the reconstruction. It was also found that applying the constraint of a monotonically expanding lesion, which makes biophysical sense, improved the reconstructions. To improve fitting of the optical properties, it is possible that a global fit of measurements at several lesion diameters could improve the accuracy and convergence of the reconstruction. Reconstruction in this scenario would simultaneously fit multiple lesions measured at different times during treatment while optimizing a single pair of optical properties for all lesions. Reconstruction of the latest measurement would still be performed separately after the global fit using the optical properties from the global fit as the starting conditions for optimization.

Only changes in the tissue scattering due to photocoagulation were considered in these simulations. While scattering is certainly a robust indicator of tissue coagulation,<sup>45</sup> changes in absorption are also evident, although the evolution during treatment may vary between individuals.<sup>34</sup> We have seen during the SBDOT studies that even small contrasts in tissue absorption can improve the reconstruction. However, systematic testing is required, both by simulation and experimentally, to evaluate if this reliably improves the reconstruction accuracy, especially considering that Lin et al.<sup>34</sup> have reported a high degree of individual variability in this parameter. Other physiological changes may occur in the prostate in response to PTT, such as increased blood flow and content. Such changes can also be included in the model by allowing for optimization of the prostate optical properties outside the lesion.

Finally, the simulations presented use cw light at only a single wavelength. Improvements to the reconstruction using frequency-domain measurements may be limited. Frequency-domain simulations showed that the phase at the largest source–detector separations changed by only a few degrees when going from a small to a large photothermal lesion. Multispectral measurements may offer a greater improvement. The scattering spectrum does not change significantly at these wavelengths. However, large differences in absorption at several wavelengths may help to constrain the fitting if a multiwavelength detection system was used. Our current system uses three wavelengths (750, 808, and 905 nm) and we will investigate the benefits of multispectral fitting for the shape-based methods.

## 5 Conclusions

These initial simulation studies indicate that shape-based transrectal DOT reconstruction is a viable approach for achieving accurate delineation of the photocoagulation boundary during focal PTT of prostate cancer to ensure safety of the rectal wall, which is a primary clinical concern. While the optical properties of the lesion could also be optimized, accurate reconstruction of

the boundary location was achieved in many cases even when the assumed optical properties were different than the actual values. Further validation and testing of this reconstruction algorithm will be tested in phantoms, *ex vivo*, and *in vivo* tissues to translate into first-in-human clinical trials.

## Disclosures

No conflicts of interest, financial or otherwise, are declared by the authors.

## Acknowledgments

This work was supported by the Collaborative Health Research Project (Grant No. 385847) jointly funded by the Canadian Institutes of Health Research and the National Science and Engineering Research Council of Canada and by the Terry Fox Research Institute (Grant No. 1022).

## References

1. S. R. Harlan et al., “Time trends and characteristics of men choosing watchful waiting for initial treatment of localized prostate cancer: results from CaPSURE,” *J. Urol.* **170**(5), 1804–1807 (2003).
2. A. L. Potosky et al., “Five-year outcomes after prostatectomy or radiotherapy for prostate cancer: the prostate cancer outcomes study,” *J. Natl. Cancer Inst.* **96**(18), 1358–1367 (2004).
3. S. E. Eggener et al., “Focal therapy for localized prostate cancer: a critical appraisal of rationale and modalities,” *J. Urol.* **178**(6), 2260–2267 (2007).
4. A. Barqawi and E. D. Crawford, “Focal therapy in prostate cancer: future trends,” *BJU Int.* **95**(3), 273–274 (2005).
5. G. Onik, “Rationale for a ‘male lumpectomy,’ a prostate cancer targeted approach using cryoablation: results in 21 patients with at least 2 years of follow-up,” *Cardiovasc. Interventional Radiol.* **31**(1), 98–106 (2008).
6. A. B. Barqawi and E. D. Crawford, “Emerging role of HIFU as a non-invasive ablative method to treat localized prostate cancer,” *Oncology* **22**(2), 123–129 (2008).
7. S. Muto et al., “Focal therapy with high-intensity-focused ultrasound in the treatment of localized prostate cancer,” *Jpn. J. Clin. Oncol.* **38**(3), 192–199 (2008).
8. L. L. Pisters, “Cryotherapy for prostate cancer: ready for prime time?” *Curr. Opin. Urol.* **20**(3), 218–222 (2010).
9. C. R. Ritch and A. E. Katz, “Prostate cryotherapy: current status,” *Curr. Opin. Urol.* **19**(2), 177–181 (2009).
10. D. J. Perekh, L. W. Chiang, and S. D. Herrell, “In vivo assessment of radio frequency induced thermal damage of kidney using optical spectroscopy,” *J. Urol.* **176**(4), 1626–1630 (2006).
11. Y. C. Chen et al., “Magnetic resonance imaging guidance for laser photothermal therapy,” *J. Biomed. Opt.* **13**(4), 044033 (2008).
12. U. Lindner et al., “Image guided photothermal focal therapy for localized prostate cancer: phase I trial,” *J. Urol.* **182**(4), 1371–1377 (2009).
13. U. Lindner et al., “Focal laser ablation for prostate cancer followed by radical prostatectomy: validation of focal therapy and imaging accuracy,” *Eur. Urol.* **57**(6), 1111–1114 (2010).
14. U. Lindner et al., “Initial results of MR guided laser focal therapy for prostate cancer,” *J. Urol.* **189**(4), E227–E228 (2013).
15. J. He et al., “Development of transrectal diffuse optical tomography combined with 3D-transrectal ultrasound imaging to monitor the photocoagulation front during interstitial photothermal therapy of primary focal prostate cancer,” *Proc. SPIE* **8578**, 85781J (2013).
16. J. He et al., “Diffuse optical tomography to monitor the photocoagulation front during interstitial photothermal therapy: numerical simulations and measurements in tissue-simulating phantoms,” *Photonics Lasers Med.* **3**(3), 241–254 (2014).
17. Z. Jiang et al., “Trans-rectal ultrasound-coupled near-infrared optical tomography of the prostate. Part II: experimental demonstration,” *Opt. Express* **16**(22), 17505–17520 (2008).

18. Z. Jiang et al., "In vivo trans-rectal ultrasound coupled trans-rectal near-infrared optical tomography of canine prostate bearing transmissible venereal tumor," *Proc. SPIE* **7174**, 71741U (2009).
19. D. Piao et al., "Alternative transrectal prostate imaging: a diffuse optical tomography method," *IEEE J. Sel. Top. Quantum Electron.* **16**(4), 715–729 (2010).
20. G. Xu et al., "Trans-rectal ultrasound-coupled near-infrared optical tomography of the prostate. Part I: simulation," *Opt. Express* **16**(22), 17484–17504 (2008).
21. H. Dehghani et al., "Near infrared optical tomography using NIRFAST: algorithm for numerical model and image reconstruction," *Int. J. Numer. Methods Biomed. Eng.* **25**(6), 711–732 (2009).
22. B. W. Pogue et al., "Implicit and explicit prior information in near-infrared spectral imaging: accuracy, quantification and diagnostic value," *Philos. Trans. R. Soc. A: Math. Phys. Eng. Sci.* **369**(1955), 4531–4557 (2011).
23. S. Srinivasan et al., "Near-infrared characterization of breast tumors in vivo using spectrally-constrained reconstruction," *Technol. Cancer Res. Treat.* **4**(5), 513–526 (2005).
24. B. Brooksby et al., "Imaging breast adipose and fibroglandular tissue molecular signatures by using hybrid MRI-guided near-infrared spectral tomography," *Proc. Natl. Acad. Sci. U. S. A.* **103**(23), 8828–8833 (2006).
25. V. Ntziachristos et al., "Concurrent MRI and diffuse optical tomography of breast after indocyanine green enhancement," *Proc. Natl. Acad. Sci. U. S. A.* **97**(6), 2767–2772 (2000).
26. P. K. Yalavarthy et al., "Structural information within regularization matrices improves near infrared diffuse optical tomography," *Opt. Express* **15**(13), 8043–8058 (2007).
27. S. R. Arridge et al., "Reconstruction of subdomain boundaries of piecewise constant coefficients of the radiative transfer equation from optical tomography data," *Inverse Prob.* **22**(6), 2175–2196 (2006).
28. O. Dorn and D. Lesselier, "Level set methods for inverse scattering," *Inverse Prob.* **22**(4), R67–R131 (2006).
29. M. Schweiger et al., "3D level set reconstruction of model and experimental data in diffuse optical tomography," *Opt. Express* **18**(1), 150–164 (2010).
30. A. N. Bashkatov et al., "Optical properties of human colon tissues in the 350–2500 nm spectral range," *Quantum Electron.* **44**(8), 779–784 (2014).
31. D. Hidovic-Rowe and E. Claridge, "Modelling and validation of spectral reflectance for the colon," *Phys. Med. Biol.* **50**(6), 1071–1093 (2005).
32. K. K. H. Wang and T. C. Zhu, "Reconstruction of in-vivo optical properties for human prostate using interstitial diffuse optical tomography," *Opt. Express* **17**(14), 11665–11672 (2009).
33. R. A. Weersink et al., "Techniques for delivery and monitoring of TOOKAD (WST09)-mediated photodynamic therapy of the prostate: clinical experience and practicalities," *J. Photochem. Photobiol. B* **79**(3), 211–222 (2005).
34. W. C. Lin, C. Buttemere, and A. Mahadevan-Jansen, "Effect of thermal damage on the in vitro optical and fluorescence characteristics of liver tissue's," *IEEE J. Sel. Top. Quantum Electron.* **9**(2), 162–170 (2003).
35. J. P. Ritz et al., "Continuous changes in the optical properties of liver tissue during laser-induced interstitial thermotherapy," *Lasers Surg. Med.* **28**(4), 307–312 (2001).
36. J. P. Ritz et al., "Optical properties of native and coagulated porcine liver tissue between 400 and 2400 nm," *Lasers Surg. Med.* **29**(3), 205–212 (2001).
37. M. G. Skinner et al., "Changes in optical properties of ex vivo rat prostate due to heating," *Phys. Med. Biol.* **45**(5), 1375–1386 (2000).
38. H. Dehghani et al., "Numerical modelling and image reconstruction in diffuse optical tomography," *Philos. Trans. R. Soc. A: Math. Phys. Eng. Sci.* **367**, 3073–3093 (2009).
39. O. Raz et al., "Real-time magnetic resonance imaging-guided focal laser therapy in patients with low-risk prostate cancer," *Eur. Urol.* **58**(1), 173–177 (2010).
40. S. W. Perry, R. M. Burke, and E. B. Brown, "Two-photon and second harmonic microscopy in clinical and translational cancer research," *Ann. Biomed. Eng.* **40**(2), 277–291 (2012).
41. A. Uchugonova et al., "Cancer-cell killing by engineered salmonella imaged by multiphoton tomography in live mice," *Anticancer Res.* **32**(10), 4331–4337 (2012).
42. M. Rodrigues, R. A. Weersink, and W. M. Whelan, "Assessment of thermal coagulation in ex-vivo tissues using Raman spectroscopy," *J. Biomed. Opt.* **15**(6), 068001 (2010).
43. J. Snyman, *Practical Mathematical Optimization: An Introduction to Basic Optimization Theory and Classical and New Gradient-Based Algorithms*, Springer Science and Business Media (2005).
44. D. Ashlock, *Evolutionary Computation for Modeling and Optimization*, Springer Publishing Company, Incorporated (2010).
45. L. C. L. Chin et al., "Radiance-based monitoring of the extent of tissue coagulation during laser interstitial thermal therapy," *Opt. Lett.* **29**(9), 959–961 (2004).

Biographies for the authors are not available.